



# Use of continuous sample translation to reduce radiation damage for XPCS studies of protein diffusion

Laurence B. Lurio,<sup>a,b,\*</sup> George M. Thurston,<sup>c</sup> Qingteng Zhang,<sup>b</sup> Suresh Narayanan<sup>b</sup> and Eric M. Dufresne<sup>b</sup>

Received 14 August 2020

Accepted 2 January 2021

Edited by U. Jeng, NSRRC, Taiwan

**Keywords:** XPCS; SAXS; protein diffusion; radiation damage; alpha crystallin.

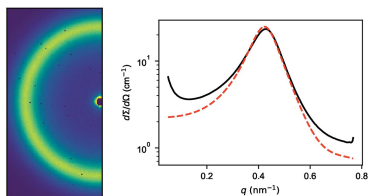
<sup>a</sup>Department of Physics, Northern Illinois University, DeKalb, IL 60115, USA, <sup>b</sup>X-ray Science Division, Argonne National Laboratory, Lemont, IL 60439, USA, and <sup>c</sup>School of Physics and Astronomy, Rochester Institute of Technology, Rochester, NY 14623, USA. \*Correspondence e-mail: llurio@niu.edu

An experimental setup to measure X-ray photon correlation spectroscopy during continuous sample translation is presented and its effectiveness as a means to avoid sample damage in dynamics studies of protein diffusion is evaluated. X-ray damage from focused coherent synchrotron radiation remains below tolerable levels as long as the sample is translated through the beam sufficiently quickly. Here it is shown that it is possible to separate sample dynamics from the effects associated with the transit of the sample through the beam. By varying the sample translation rate, the damage threshold level,  $D_{\text{thresh}} = 1.8$  kGy, for when beam damage begins to modify the dynamics under the conditions used, is also determined. Signal-to-noise ratios,  $R_{\text{sn}} \geq 20$ , are obtained down to the shortest delay times of 20  $\mu\text{s}$ . The applicability of this method of data collection to the next generation of multi-bend achromat synchrotron sources is discussed and it is shown that sub-microsecond dynamics should be obtainable on protein samples.

## 1. Introduction

X-ray photon correlation spectroscopy (XPCS) provides a unique window on molecular scale dynamics in materials, currently with a sensitivity to timescales from milliseconds to seconds (Sutton, 2008; Grübel *et al.*, 2008; Leheny, 2012; Sinha *et al.*, 2014; Sandy *et al.*, 2018). A new generation of multi-bend achromat (MBA) synchrotron sources are becoming available, such as ESRF-EBS, MAX IV, PETRA IV and the APS-U. These will provide high brightness and nearly diffraction-limited X-ray beams which should enable XPCS measurements of molecular scale diffusion with sub-microsecond time resolution. Such machines could enable studies of biomaterials at physiologically relevant timescales, but X-ray induced damage remains a concern. XPCS requires a high-intensity beam and measurements of dynamics are sensitive to both radiation-induced structural changes as well as other factors such as cross linking or ionization which might modify dynamics without obvious signatures in the static structure.

Radiation damage to samples is of critical importance in the X-ray and electron microscopy communities and a number of works have reviewed both the mechanisms of radiation damage and experimental strategies to reduce such damage (Wang *et al.*, 2018; Garman & Weik, 2017; Costa *et al.*, 2016; Ueno *et al.*, 2019; Garrison, 1987; Meisburger *et al.*, 2013; Egerton, 2019; Polsinelli *et al.*, 2017; Hopkins & Thorne, 2016; Blakeley *et al.*, 2015; Ryan *et al.*, 2018; Jeffries *et al.*, 2015; Allan *et al.*, 2013; Brooks-Bartlett *et al.*, 2017; Garman & Weik,



OPEN ACCESS

2015; Massover, 2007; Kirby *et al.*, 2016). Radiation damage in protein samples has been studied by the macromolecular crystallography (MX) and small-angle X-ray scattering (SAXS) communities. MX is relatively tolerant to damage, with acceptable doses in the hundreds of kGy (Blakeley *et al.*, 2015) before significant changes to protein structure occur. SAXS can be much more sensitive to radiation effects, since protein aggregation occurs at lower doses where it gives rise to changes in the shape of the scattering curve at low angle. SAXS studies have shown that aggregation occurs in the range from several hundred to several thousand Gy depending on factors such as the protein type and addition of radio-protectants (Kuwamoto *et al.*, 2004; Brooks-Bartlett *et al.*, 2017). Common strategies to reduce damage in protein measurements are cryo-cooling, the addition of radio-protectants, and moving the sample through the beam to expose fresh sample, either through sample flow, typically done in SAXS, or sample translation, which is more common in MX (Shotton *et al.*, 1998; Jeffries *et al.*, 2015; Blakeley *et al.*, 2015; Kirby *et al.*, 2016; Ueno *et al.*, 2019).

Since XPCS is a probe of dynamics, sample translation could obviously interfere with the measurement. One solution that has been employed for performing XPCS on radiation-sensitive soft matter samples has been to measure for short intervals on a single spot, and then collect data on a large number of spots. This data collection scheme has been implemented for the case of speckle visibility, a variant of XPCS, by Verwohlt *et al.* (2018) and Möller *et al.* (2019). Another strategy that has been adopted has been to flow the sample through the beam (Fluerasu *et al.*, 2008). This method has mainly been employed when the effects of flow were the subject of the study, as the gradients in velocity introduced by the presence of shear can complicate the analysis, although methods have been developed to mitigate the effect of velocity gradients (Kirby *et al.*, 2016).

In the present work, we have adopted a different strategy. The sample is enclosed in a capillary which is continuously translated through the beam during the measurement. The effects of sample translation are then corrected for in the time correlation function,  $g_2$ . This method yields values for the signal-to-noise ratio to sample damage comparable with the alternative of measuring a large number of independent sample spots for a short exposure time. It is significantly more efficient, however, since it only requires a continuous motion of the sample rather than measuring of the order of a million independent sample positions. We apply this technique to the study of the eye-lens protein alpha crystallin; but we believe that it should be widely applicable to a range of biological and soft materials. We have designed a sample translation system with precise velocity control to avoid the addition of noise due to motion jitter. By examining the time correlation function of the sample as a function of translation speed we obtain a threshold dose for X-ray effects on diffusive dynamics of a highly concentrated protein solution.

We consider here measurements on concentrated alpha crystallin proteins originally measured by Vodnala *et al.* (2018). We show that it is possible to perform measurements

of dynamics down to sub-millisecond time resolution without exceeding a dose where X-ray damage significantly modifies sample dynamics, and designate this the critical dose. The implications of this technique for the future of XPCS measurements using the coming generation of MBA synchrotron sources is also explored. In particular, we show that, in spite of the strong sensitivity to X-ray damage, the increased flux available at MBA sources will provide a significant advantage which can be used to extend the range of measurements on biomaterials down to sub-microsecond timescales.

## 2. Experiment

Samples of concentrated bovine alpha crystallin were enclosed in thin-walled 1 mm outer-diameter borosilicate glass capillaries (Charles Supper) aligned along the vertical. Proteins were prepared in a 0.1 M sodium phosphate buffer, pH 7.1, that contained 20 mM dithiothreitol (DTT) as an antioxidant, as described previously (Thurston, 2006). The protein solutions were then concentrated via centrifugation using filters (Amicon Ultra 0.5 ml). Samples were illuminated with a partially coherent X-ray beam defined by slits in the horizontal direction and focused in the vertical direction using a beryllium compound refractive lens (CRL). Vertical focusing was employed to match the speckle size of the coherent diffraction pattern in the vertical direction to the 76  $\mu\text{m}$  pixel size on the Rigaku XSPA-500k camera (Zhang *et al.*, 2021) located 3.93 m downstream of the sample. The speckle size in the horizontal direction was smaller than the pixel size resulting in a reduced contrast in the X-ray speckle pattern. Horizontal focusing was not practical due to the large source size in the horizontal direction. A translation stage moved samples vertically through the X-ray beam with translation rates which varied from 2.5  $\text{mm s}^{-1}$  to 0.08  $\text{mm s}^{-1}$ . Samples were translated vertically for 10 mm then moved horizontally by the beam width (15  $\mu\text{m}$ ) and then translated back down in a raster pattern. Only the central 0.60 mm of the circular cross-section capillary was used, allowing for 40 stripes per capillary.

The sample translation stage is an Aerotech brushless servo motor driven linear stage (ANT95L-025). Since the stage is used in the vertical orientation, air pressure is tuned to counter the force of gravity so it stays balanced by the upward air pressure that counteracts the atmospheric pressure and the payload on the stage. The stage is controlled using an Aerotech Ensemble HLe and operates in a closed-loop manner using a built-in linear encoder that has a 2 nm positional resolution and a 10–20 nm bi-directional positional repeatability. The control algorithm uses dual position and velocity servo loops to yield a very smooth motion profile with a velocity error that is less than 10% of the commanded velocity profile. In order for the motion to not adversely affect the shape of the correlation function, it is imperative that the motion be a continuous profile such as from a servo motor driven linear stage. A previous implementation of the sample translation based on a stepper motor driven stage introduced

undesirable oscillations in the correlation function that resulted from the steps from the stepper motor.

### 3. Results and discussion

The normalized intensity–intensity time autocorrelation function is defined by

$$g_2(\mathbf{q}, \tau) = \langle I(\mathbf{q}, t) I(\mathbf{q}, t + \tau) \rangle / \langle I(\mathbf{q}) \rangle^2. \quad (1)$$

Here  $I(\mathbf{q}, t)$  is the scattered intensity within a detector pixel at wavevector  $\mathbf{q}$  and time  $t$  and  $I(\mathbf{q}, t + \tau)$  is the intensity within the same pixel after time delay  $\tau$ . The average denoted by  $\langle \dots \rangle$  is performed over both the initial time,  $t$ , and over all pixels with equivalent values of  $q$ . For non-oriented samples, which we consider here, the scattering only depends on the magnitude of  $\mathbf{q}$  so that all pixels with the same value of  $q$  are equivalent. In the absence of sample motion,  $g_2$  can be directly related to the intermediate scattering function of the sample,  $f(q, \tau)$ , via

$$g_2(q, \tau) = 1 + \beta f(q, \tau)^2. \quad (2)$$

Here  $\beta$  is the optical contrast.

The effect of sample transit through the focus of a Gaussian beam has been derived in the context of dynamic light scattering (Chowdhury *et al.*, 1984; Taylor & Sorensen, 1986). Consider a focused Gaussian beam with an intensity profile at its focus given by

$$I(z) = I_0 \exp(-z^2/2\sigma^2). \quad (3)$$

Here, we define the  $z$  axis along the vertical direction transverse to the propagation of the beam. For a homodyne experiment in the far field limit the time autocorrelation function is modified to become

$$g_2(\tau) = 1 + \beta f(\tau)^2 \exp(-v_z^2 \tau^2 / 4\sigma^2). \quad (4)$$

Note that the correction in equation (4) is independent of  $q$ . An important feature of this relationship is that  $\sigma$  is the size of the Gaussian focus, not the beam size at the sample location. Thus, translating the sample along the propagation direction of the beam will not change the decorrelation time, even though it changes the beam size on the sample. The dependence of decoherence on the focus size seems counter-intuitive. It can be understood in terms of the beam wavefront curvature introducing a phase shift which changes as the sample translates. This result has been rigorously demonstrated both theoretically and verified experimentally in the context of dynamic light scattering (Taylor & Sorensen, 1986). In the context of XPCS, the falloff in the correlation function due to transit of the sample through the beam has been noted by a number of previous authors (Vodnala *et al.*, 2018; Lhermitte *et al.*, 2017; Busch *et al.*, 2008; Gabriel *et al.*, 2015).

Autocorrelation functions were first measured for internally static samples of silica aerogel [ $f(\tau) = 1$ ] translated through the X-ray beam at several different velocities. The resulting  $g_2$  functions are shown in Fig. 1. The dashed lines in the figures represent a fit to the form of equation (4). Here  $\beta$  was fixed to

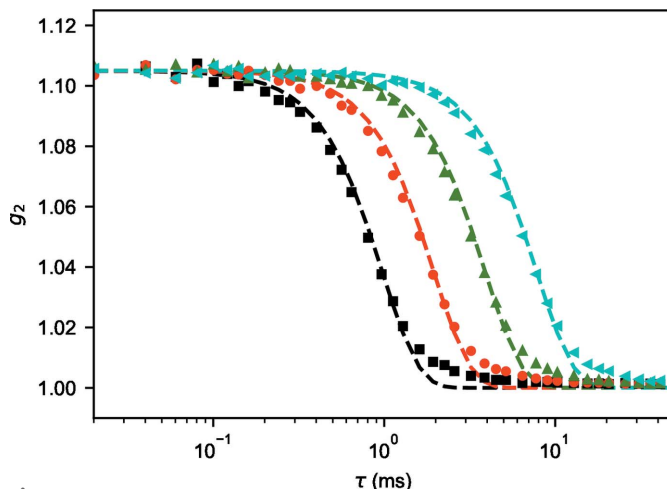


**Figure 1**  
Fit of the focus size,  $\sigma$ , to the time dependence of  $g_2$  for aerogel using equation (4). Aerogel velocities are  $2 \text{ mm s}^{-1}$  (black square),  $1 \text{ mm s}^{-1}$  (red circle),  $0.5 \text{ mm s}^{-1}$  (green up triangle) and  $0.25 \text{ mm s}^{-1}$  (cyan left triangle).

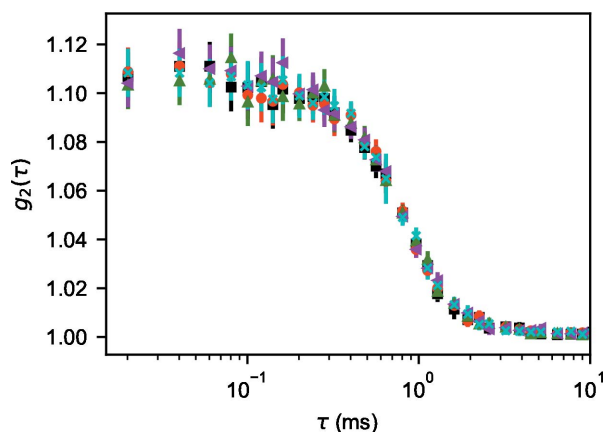
the  $\tau = 0$  limit of the data, and a single value of  $\sigma$  was fit to all three data sets using nonlinear least-square regression with the *lmfit* package in Python (<https://lmfit.github.io/lmfit-py/>). The fit yielded  $\sigma = 0.97 \pm 0.02 \text{ }\mu\text{m}$  for the vertical RMS beam focus. A calculation of the diffraction-limited beam focus width for the beryllium CRL based on Singer & Vartanyants (2014) predicts a beam size at focus of  $0.68 \text{ }\mu\text{m}$ , which is somewhat smaller than the measured value. This may result from imperfections in the focusing optic, or reductions in the beam coherence due to interactions with beamline optics upstream of the lens. The small misfit in the tail of the correlation function at long times may result from these imperfections in the beam focus.

As noted by Vodnala *et al.* (2018) the intensity falloff due to sample translation is caused by a reduction in overlap of the scattering volumes over the measured delay time. One would not expect the measured correlation functions to depend on the angle of scattering relative to the translation direction. To verify this we have examined the scattering from a static aerogel sample translated at  $2 \text{ mm s}^{-1}$  as a function of azimuthal angle relative to the translation direction. Fig. 2 shows averages of  $g_2$  functions for this sample over five evenly spaced angular ranges with the translation direction at  $90^\circ$ . The absence of any azimuthal dependence indicates that there is no directional dependence introduced to the correlation functions due the translation.

The time-averaged scattering from a concentrated alpha crystallin suspension and the circular average of the scattering are shown in Fig. 3. The circularly averaged data have been normalized to absolute scattering cross-section per unit volume,  $(1/V)(d\sigma/d\Omega)$ , using

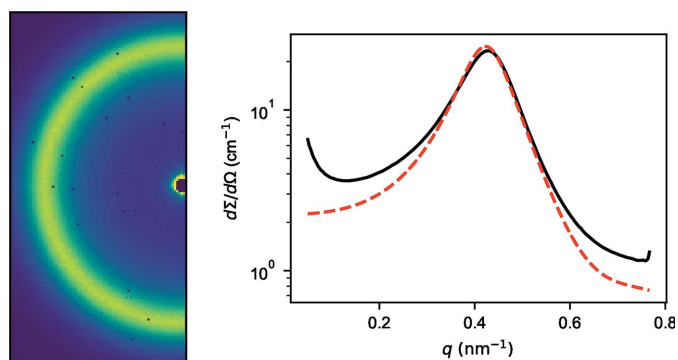
$$\frac{1}{V} \frac{d\sigma}{d\Omega} = \frac{I_{\text{det}}}{I_t \Lambda d\Omega}. \quad (5)$$

Here  $I_t$  is the direct beam intensity transmitted through the sample,  $I_{\text{det}}$  is scattered intensity in a detector pixel of angular


**Figure 2**

Azimuthal dependence of  $g_2$  from aerogel at a translation speed of  $2 \text{ mm s}^{-1}$  and scattering wavevector of  $q = 0.096 \text{ nm}^{-1}$ . Azimuthal angles:  $54^\circ$  (cyan crosses),  $125^\circ$  (black squares),  $198^\circ$  (red circles),  $270^\circ$  (green up triangles),  $342^\circ$  (magenta left triangles).

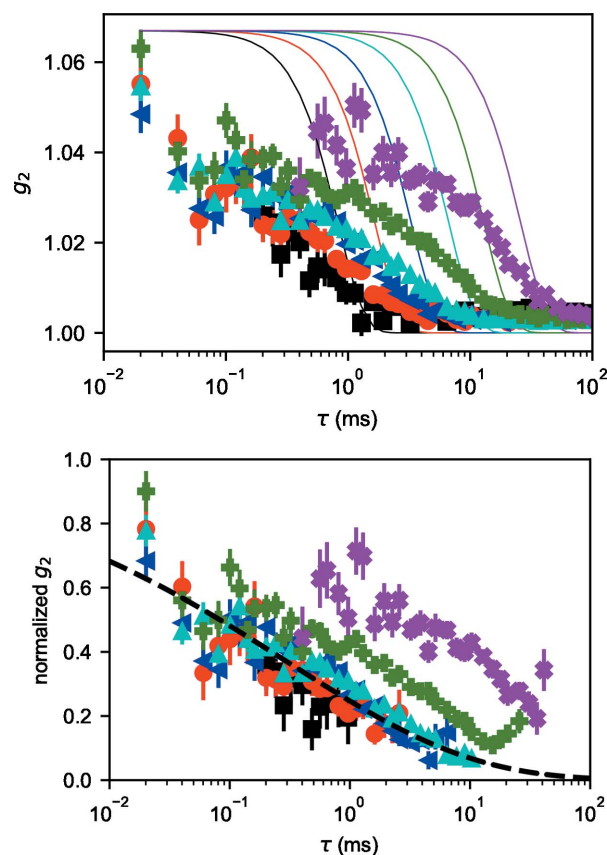
size  $d\Omega$ , and  $\Lambda$  is the sample thickness. Note that some regions of Fig. 3 are masked to remove parasitic scattering or bad camera pixels. The excess scattering at small  $q$  likely results from parasitic scattering from the incident beam which could not be completely blocked in the focusing geometry used for the experiment. The dashed red line in Fig. 3 depicts a fit to the scattering using a polydisperse hard sphere model (Vrij, 1979; Griffith *et al.*, 1987) with a hard sphere volume fraction  $\phi_{\text{HS}} = 56\%$ , polydispersity 18%, hard sphere radius  $r_d = 6.3 \text{ nm}$  and hydrodynamic radius  $r_y = 7.8 \text{ nm}$ . This model approximates the alpha crystallin form factor with a uniform sphere, so it cannot fit the large  $q$  scattering which reflects the scattering from the protein subunits. We chose to optimize the fits to the structure factor only in the vicinity of the peak, since the main goal was to obtain a value for the volume fraction based on a hard sphere model. Only the overall amplitude and volume fraction were varied in this fit, with the remaining parameters fixed based on the results from Vodnala *et al.* (2018) which used identical samples. Dynamics measurements used data from the ring of scattering in the range  $0.35 \text{ nm}^{-1} < q <$


**Figure 3**

(Left) Scattering from a concentrated alpha crystallin suspension. (Right) Circular average of alpha crystallin scattering: scattering cross section for alpha crystallin (black solid line); fit to polydisperse hard sphere model (red dashed line).

$0.50 \text{ nm}^{-1}$  where the average scattering cross section per unit volume was  $(1/V)(d\sigma/d\Omega) = 18 \text{ cm}^{-1}$ .

Time correlation functions from these samples measured over a range of sample translation speeds ranging from  $2.5 \text{ mm s}^{-1}$  to  $0.08 \text{ mm s}^{-1}$  are shown in Fig. 4. The X-ray dose absorbed by each sample will vary as the inverse of the translation speed. The solid lines in the figure indicate the expected decay due to just the beam transit from equation (4). Fig. 4 shows the data corrected for the beam transit effect. Note that, at long times,  $\exp(-v_z^2\tau^2/4\sigma^2)$  is nearly zero and retrieving the corrected  $f(\tau)$  from equation (4) can lead to points with excessively large error bars. Consequently, points with fractional error bars larger than 10% were excluded. In the absence of damage all the data points should lie on the same curve in Fig. 4. Data at translation speeds of  $2.5 \text{ mm s}^{-1}$ ,  $1.25 \text{ mm s}^{-1}$  and  $0.63 \text{ mm s}^{-1}$  and  $0.31 \text{ mm s}^{-1}$  appear to lie along a single curve, and are reasonably well approximated by a stretched exponential curve  $g_2(t) = 1 + \beta \exp[-2(t/\tau)^\gamma]$  with  $\tau = 3.5 \pm 0.4 \text{ ms}$  and  $\gamma = 0.28 \pm 0.02$ . Stretched exponential behavior is plausible for a highly concentrated protein suspension (Hunter & Weeks, 2012). The observed dynamics


**Figure 4**

(Top) Time correlation functions,  $g_2(\tau)$ , for various translation speeds:  $2.5 \text{ mm s}^{-1}$  (black squares);  $1.25 \text{ mm s}^{-1}$  (red circles);  $0.63 \text{ mm s}^{-1}$  (blue sideways triangles);  $0.31 \text{ mm s}^{-1}$  (cyan up triangles);  $0.16 \text{ mm s}^{-1}$  (green crosses);  $0.08 \text{ mm s}^{-1}$  (magenta Xs). Lines indicate the expected decay due to just the beam transit from equation (4). (Bottom) Time correlation functions,  $g_2(\tau)$ , corrected for the effects of translation given in equation (4). Points with uncertainties larger than 10% are not shown. The dashed line is a stretched exponential fit to the data from just the three fastest translation speeds.

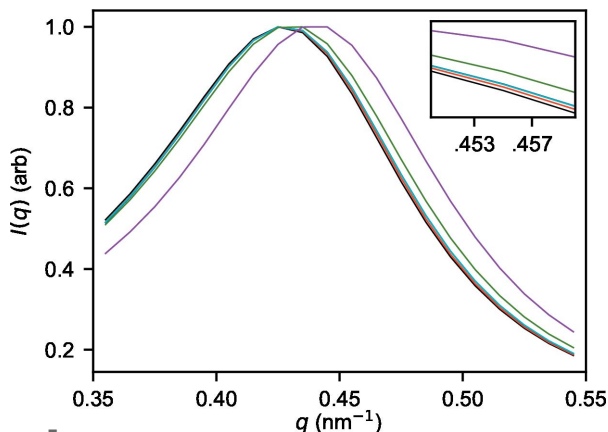


**Figure 5** Static scattering from alpha crystallin versus wavevector  $q$  for various translation speeds. The inset shows a close up of the peak region.  $2.5 \text{ mm s}^{-1}$  (black);  $1.25 \text{ mm s}^{-1}$  (red);  $0.63 \text{ mm s}^{-1}$  (blue);  $0.31 \text{ mm s}^{-1}$  (cyan);  $0.16 \text{ mm s}^{-1}$  (green);  $0.08 \text{ mm s}^{-1}$  (magenta).

for the data sets with translation speeds below  $0.31 \text{ mm s}^{-1}$  deviate from the remainder of the data. We take this as an indication of beam-induced damage.

The onset of damage at the same translation speed is also visible in the static scattering patterns. Figure 5 shows the scattering intensity versus wavevector  $q$  for the same set of samples. The static structure is nearly identical for the first three samples but begins to shift to higher  $q$  for the slower moving samples subject to higher doses. The peak in the structure factor is an indication of the protein nearest neighbor distance. We postulate that a shift towards higher  $q$  indicates an attractive interaction or possibly physical or chemical bonding between the proteins which causes aggregation. This aggregation could then plausibly explain the slowdown in dynamics.

The radiation dose delivered to a sample is given by (Hopkins & Thorne, 2016)

$$D = \frac{\phi t A E_\gamma}{\rho l}. \quad (6)$$

Here  $\phi$  is the flux density ( $\text{photon s}^{-1} \text{ m}^{-2}$ ),  $t$  the exposure time,  $A$  the fraction of the incident energy absorbed,  $E_\gamma$  the photon energy,  $\rho$  the mass density and  $l$  the X-ray path length through the sample. Consider a beam of cross section  $h \times w$  with  $h$  the beam height and  $w$  the beam width, and assume the sample translates through the beam with vertical velocity  $v_z$ . In this case the beam, having flux density  $\phi = I_0/hw$ , moves across the sample in time  $t = h/v_z$ . Here  $I_0$  is the incident intensity in  $\text{photon s}^{-1}$ . If we consider a thin section at the front of the sample of thickness  $dl$ , then  $A = dl/\Lambda$  with  $\Lambda$  the X-ray absorption length. We then obtain, for the dose in Gy delivered to the front of the sample,

$$D = \frac{I_0 E_\gamma}{w v_z \Lambda \rho}. \quad (7)$$

The dose is independent of the vertical beam size but only depends on the translation velocity  $v_z$ . The dose will vary over the sample with a more intense dose at the center of the beam

and the front of the sample. The slit that defines the horizontal extent of the illuminated part of the sample is located  $0.71 \text{ m}$  in front of the sample. At the beam energy of  $10.9 \text{ keV}$ , this slit only diffracts a small amount from its initial size of  $w = 15 \text{ }\mu\text{m}$  out to  $w = 15.8 \text{ }\mu\text{m}$  at the sample position. This generates a small non-uniformity near the edges of the diffraction pattern. The X-ray attenuation length of  $\Lambda = 2.27 \text{ mm}$  leads to a 30% decrease in intensity between the back and front of the  $0.8 \text{ mm}$ -thick sample at its thickest point in the center of the capillary. Since these effects are small we use equation (7) for estimating the dose throughout the sample.

To calculate the absorbed dose, we need to find the sample density and attenuation length. The sample density is given by

$$\rho = \phi_p / \bar{v}_p + (1 - \phi_p) / \bar{v}_b. \quad (8)$$

Here  $\phi_p$  is the fraction of the volume occupied by protein,  $\bar{v}_p \simeq 0.71 \text{ ml g}^{-1}$  the partial specific volume typical of globular proteins (Van Holde *et al.*, 2006) and  $\bar{v}_b$  is the partial specific volume of the buffer. We use  $\phi_p = \phi_{\text{HS}} (m_p / v_p) \bar{v}_p$ . Here  $m_p = 800000 \text{ g mole}^{-1}$  is the protein molecular weight for the quaternary alpha crystallin oligomers (Ryazantsev *et al.*, 2018) and  $v_p = (4\pi/3) r_p^3$  is the protein hard sphere volume. For the measured  $\phi_{\text{HS}} = 0.56$  we obtain  $\phi_p = 0.26$ . For the buffer we determined  $\bar{v}_b = 981 \text{ m}^3 \text{ kg}^{-1}$  from the composition ( $0.1 \text{ M PO}_4^{3-}$ ,  $0.167 \text{ M Na}^+$ ,  $0.133 \text{ M H}^+$ ,  $0.02 \text{ M C}_4\text{H}_{10}\text{O}_2\text{S}_2$  and  $0.0014 \text{ M C}_7\text{H}_5\text{NaO}_2$ ). This determined the sample density of  $1.12 \times 10^3 \text{ kg m}^{-3}$ . The mass absorption coefficient was then calculated for a 3:1 ratio of alpha-A to alpha-B crystallin (Srinivas *et al.*, 2008) using the amino acid sequences corresponding to the UniProtKB accession numbers P02470 for bovine alpha-A crystallin and P02510 for bovine alpha-B crystallin (UniProt, 2019), combined with atomic absorption coefficients from the *XrayDB* Python package (<https://github.com/xraypy/XrayDB>). For the incident beam intensity  $I_0 = 1.2 \times 10^{10} \text{ photon s}^{-1}$ , the dose at velocity  $v_z$  is given by  $D v_z = 547 \text{ Gy mm s}^{-1}$  at the front of the sample in the center of the beam. Noticeable changes to the dynamics occur for velocities slower than  $v_z \leq 0.31 \text{ mm s}^{-1}$ . Based on this, we calculate a damage dose threshold of  $D_{\text{crit}} = 1.8 \text{ kGy}$ . We note that experiments reported by Vodnala *et al.* (2018) were performed at doses as high as  $17 \text{ kGy}$ ; the discrepancy between those measurements and the current damage threshold result will be discussed in further detail below.

If we assume that the primary damage mechanism is a two-step process, where ionizing radiation produces free radicals in solution which then diffuse to and react with proteins, one can then try to rationalize the critical dose based on an estimate of the ratio of free radicals to proteins. The primary radicals produced by ionizing radiation correspond to the species  $\text{H}_2\text{O}_2$ ,  $\text{H}_2$ ,  $\text{OH}$ ,  $\text{H}$ ,  $\text{e}^-$  and  $\text{H}^+$ . The rate of production of each type of radical is characterized by its ‘G’ number which gives the number of radicals per 100 eV absorbed dose. For the main radiolysis products of water the G number is approximately 2.8 (Garrison, 1987). Based on this we estimate approximately 0.4 of each radiolysis product per protein at the critical dose.

In order to quantify the effect of damage on the proteins we modeled the intermediate scattering function as the sum of a stretched exponential with amplitude  $1 - A$  and a slower exponential decay due to aggregated protein with amplitude  $A$ ,

$$f(\tau) = (1 - A) \exp[-(t/\tau)^\gamma] + A \exp(-t/\tau_2). \quad (9)$$

We assumed that the damage resulted in aggregation based on the previous results of Kuwamoto *et al.* (2004) and the expectation that slower dynamics would most likely result from aggregates. This conjecture could not be confirmed from small-angle scattering as the parasitic scattering from the focusing optic made it impossible to extract reliable scattering information at very small wavevectors.

Fits to the motion-corrected and normalized  $g_2$  functions for the measured data with velocities below  $1.25 \text{ mm s}^{-1}$  are shown in Fig. 6. The model in equation (9) does a good job of describing the data over the range of measured speeds. The parameters for the stretched exponential were obtained from the previous fits and not varied. Fig. 7 shows the resulting values for  $A$  and  $\tau_2$ . These are fit to power laws as a function of dose, with  $A \simeq D^{0.30 \pm 0.07}$  and  $\tau_2 \simeq D^{0.90 \pm 0.2}$ . While we do not have a rationale for this power law dependence on dose, the observation that the amplitude does not go to zero for a translation velocity of  $0.31 \text{ mm s}^{-1}$  implies that likely some damage persists even at the nominal threshold dose. Since, however, for lower doses the relaxation time of the nominal damage component closely approaches the relaxation time of the undamaged sample, the separation of damaged and non-damaged sample becomes difficult, and the fit of equation (9) may not be justified. In particular, in the glassy state, the protein dynamics are already significantly slowed by protein–protein interactions. Thus, it is possible that the additional interactions due to damage simply become of the same magnitude or smaller than the near neighbor hard sphere interactions already occurring in the glassy state. It may be that in more dilute systems, where glassy protein interactions are negligible, the threshold for detectable damage could be lower.

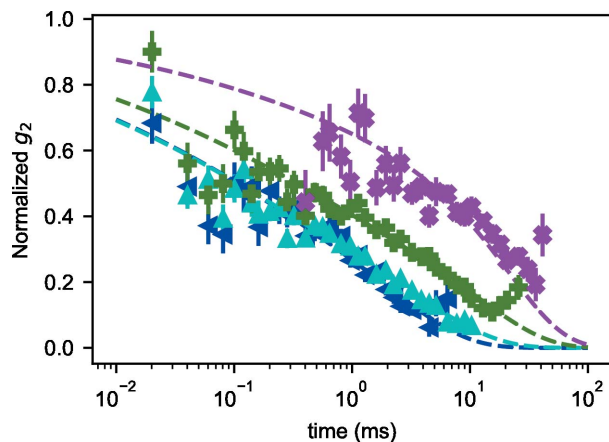


**Figure 6** Fits to  $g_2$  using the damage model described in the text.  $0.63 \text{ mm s}^{-1}$  (blue sideways triangles);  $0.31 \text{ mm s}^{-1}$  (cyan up triangles);  $0.16 \text{ mm s}^{-1}$  (green crosses);  $0.08 \text{ mm s}^{-1}$  (magenta Xs). Dashed lines depict fits.

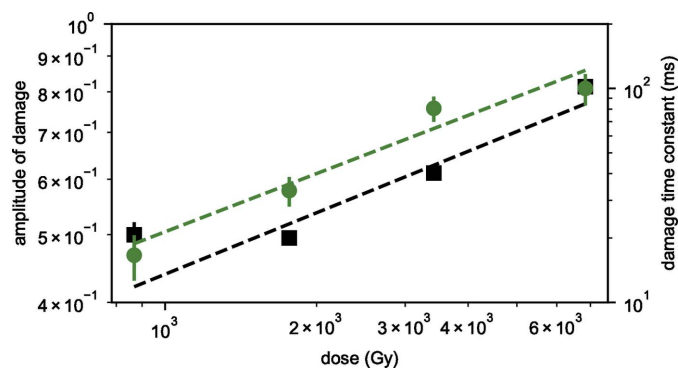


**Figure 7** (Left axis, black squares) Amplitude of the damage term contribution to  $g_2$  using the damage model described in the text. The dashed black line is a power law fit with slope  $0.30 \pm 0.07$ . (Right axis, green circles) Relaxation times determined from the damage term contribution to  $g_2$  using the damage model described in the text. The dashed green line is a power law fit with slope  $0.90 \pm 0.2$ .

The present results for the damage threshold are apparently inconsistent with the prior results of Vodnala *et al.* (2018) who found a damage threshold approximately ten times higher ( $20 \text{ kGy}$ ). Consequently we consider factors which might lead to the difference between that work and the present one. While the measurements of Vodnala *et al.* (2018) were made at lower energy ( $7.35 \text{ keV}$ , versus  $10.9 \text{ keV}$  in the present work) it is expected that for X-ray induced radiation damage the primary damage mechanism is ionization due to secondary photoelectrons, and this ionization damage should only depend on the total absorbed dose, not the energy (Egerton, 2019). A significant difference between the previous and present work is that the incident flux (absorbed dose per unit time) in Vodnala *et al.* (2018) was approximately five times smaller than in the present work, even though the total dose was ten times larger. One possible explanation for a dependence of damage on flux could be due to free radicals diffusing out of the illuminated sample area. The illuminated sample region is a small spot with vertical height,  $h$ , defined by the focus size and horizontal width  $w$  defined by the horizontal defining slit. Since the beam sweeps along the vertical direction as the sample moves, half the free radicals diffusing along the vertical direction diffuse back into the region yet to be illuminated. For simplicity we consider solely one-dimensional diffusion out of the beam plane along the horizontal direction. This overestimates the effect of radicals diffusing back into the translation path, since it does not consider any diffusion of the radicals along the vertical direction moving opposite to the motion, radicals which would also leave the beam path. Assuming a typical diffusion coefficient for free radicals in water of the order of that for molecular hydrogen,  $5 \times 10^{-9} \text{ m}^2 \text{ s}^{-1}$  (Ferrell & Himmelblau, 1967), one finds that the radicals would diffuse in one dimension approximately  $45 \mu\text{m}$  during the  $0.4 \text{ s}$  illumination time used by Vodnala *et al.* (2018). This is to be compared with the  $20 \mu\text{m}$  horizontal beam size used in that experiment. Thus a substantial fraction of the free radicals would have had time to leave either the scattering volume or the regions yet to be illuminated, before interacting

with proteins. In the present work, the sample was illuminated for 7 ms at the translation speed corresponding to the critical dose ( $0.31 \text{ mm s}^{-1}$ ). During that time free radicals would diffuse of the order  $6 \mu\text{m}$ , whereas the beam width was  $w = 15 \mu\text{m}$ . Thus, in the present case, the dose estimates should more accurately represent the dose received by the proteins, while for the case of Vodnala *et al.* (2018) the applied dose represents a substantial overestimate of the dose received. Other diffusion processes, such as diffusion of fresh anti-oxidant into the illuminated volume, or diffusion of damaged protein out of the illuminated volume, could also affect the dose estimate, but significantly smaller diffusion coefficients are associated with these mechanisms.

#### 4. Discussion

For the slowest translation speed that did not show radiation damage effects,  $0.31 \text{ mm s}^{-1}$ , the signal-to-noise ratio was  $R_{\text{sn}} = 20$ . This indicates that with the current method of continuous sample translation it is possible to collect high-quality data down to the limiting exposure time of the camera of  $20 \mu\text{s}$ . This is currently the fastest continuous readout megapixel camera available for XPCS (Kleczek *et al.*, 2019). This dataset required 5544 s of accumulation time. Data at longer delay times could have been acquired, if needed, by merging datasets together using attenuated flux and slow translation speed; however, the current  $g_2$  had decayed to less than 10% of its initial value before the data were cut off by the sample translation so that patching datasets together was not necessary.

The development of a new class of synchrotron sources based on MBAs, such as ESRF-EBS, MAX IV, PETRA III and the APS-U, will lead to increases in available coherent flux by several orders of magnitude (Eriksson *et al.*, 2014). An important question is the degree to which XPCS measurements on biomaterials will benefit from the increased flux. There are several factors which give reason for optimism that the increased coherent flux can be effectively utilized. The significant reduction in horizontal source size will allow for sample illumination by fully coherent X-ray beams, rather than the partially coherent X-ray beams used in the present study. Since the incoherent fraction of the beam causes sample damage without contributing to the useful signal, increasing the beam coherence can only provide an improvement in measurement quality.

Increases in total flux and in the flux density of focused beams can have positive effects due to more scattered intensity, but also negative effects due to more sample damage. An important distinction between XPCS measurements and conventional scattering is the scaling of  $R_{\text{sn}}$  with flux. For conventional X-ray experiments,  $R_{\text{sn}} \simeq \sqrt{IT}$  with  $I$  the incident intensity and  $T$  the total measurement duration. By contrast, since XPCS experiments count two-photon correlations,  $R_{\text{sn}} \simeq I\sqrt{T}$ . Thus, a factor of two increase in flux leads to a factor of four reduction in required counting time so that more flux reduces the total sample damage at fixed  $R_{\text{sn}}$ .

Another possible advantage will be the availability of coherent X-rays at higher energies. While higher energy has the advantage that it reduces X-ray damage and decreases beam attenuation, reductions in the solid angle of scattering and limitations due to finite longitudinal coherence can offset these gains. Details of these issues are discussed by Möller *et al.* (2019) who have concluded that, in the balance, high energy yields improvements in  $R_{\text{sn}}$  as long as the sample thickness can be increased to match the increased attenuation length.

To make these issues concrete we have calculated the expected signal-to-noise ratio achievable for parameters that will be available at the coherent SAXS beamline at 8-ID-I after the APS-U upgrade. These estimates give confidence that XPCS measurements will provide access to sub-microsecond dynamics of biomaterials while not exceeding the damage thresholds estimated in the present work.

We have demonstrated that the coherent flux currently available at the sector 8-ID-I beamline of the APS is sufficient to measure dynamics in protein suspensions down to timescales of  $20 \mu\text{s}$ . This limit is set by the readout of the XSPA-500k camera. While highly concentrated protein solutions yield interesting dynamic phenomena at these and longer timescales, the natural timescale appropriate to the study of protein dynamics is of the order of the time required for a protein to diffuse by its own radius,  $\tau_s = \pi\eta r^3/k_B T$ . Here  $r$  is the protein radius,  $k_B$  Boltzmann's constant, and  $\eta$  the dynamic viscosity of the fluid. For alpha crystallin in water this time scale comes out to 170 ns. More realistic biological environments would likely have higher viscosities than pure water and slower dynamics due to crowding (Dix & Verkman, 2008) so that the most relevant time scales are likely in the microsecond regime. In order to access such short time dynamics, faster detectors are clearly required.

The XSPA-500k detector is built on the UFXC detector, which is capable of a faster 'burst' mode of operation in which the on-pixel counting registers are used to store a short time-series of two-bit count data (Zhang *et al.*, 2018). In this mode the camera can measure correlation functions down to timescales as short as 830 ns. This capability comes at the cost of a reduction in duty cycle to 0.85% live time (Zhang *et al.*, 2018). While this mode of operation is not currently available in the commercial version of this detector built by Rigaku, since it is built on the same hardware such a mode is likely to become available in the near future. Based on the  $R_{\text{sn}}$  determined above, this readout mode would have too low a duty cycle to be practical with the current APS for protein measurements. We show below that with the APS-U adequate  $R_{\text{sn}}$  can be achieved in this mode while still maintaining acceptable levels of sample damage as long as continuous sample translation is employed.

A discussion of how to optimize XPCS experiments for damage susceptible biological samples has been presented by Möller *et al.* (2019). Based on these considerations we calculate  $R_{\text{sn}}$  for an experiment similar to the one described above, but using the design parameters for the 8-ID coherent SAXS beamline at the APS-U. A summary of the values used is given

**Table 1**  
Parameters for APS-U and (present APS) XPCS measurement.

Parameter	Value	Units	
$q_{\min}$	0.35	nm <sup>-1</sup>	Minimum $q$
$q_{\max}$	0.50	nm <sup>-1</sup>	Maximum $q$
$r_{\text{det}}$	12.0 (3.9)	m	Detector distance
$d_{\text{pix}}$	76.0	μm	Detector pixel size
$E$	23.7 (10.9)	keV	Beam energy
$\Delta E/E$	$3.00 \times 10^{-5}$ ( $3.30 \times 10^{-4}$ )		Si(311) monochromator
$I_0$	$1.20 \times 10^{12}$ ( $1.30 \times 10^{10}$ )	photon s <sup>-1</sup>	Incident flux
$\beta$	0.47 (0.067)		Contrast
Duty cycle	0.85% (100%)		
$t_{\text{exp}}$	0.83 (20)	μs	Exposure time
$T$	$7.20 \times 10^3$ ( $5.54 \times 10^3$ )	s	Experiment duration
$N_{\text{exp}}$	$7.45 \times 10^7$ ( $2.77 \times 10^8$ )		Number of exposures
$N_{\text{pix}}$	85 960 (157 500)		Number of detector pixels
$(1/V)(d\Sigma/d\Omega)$	18	cm <sup>-1</sup>	Cross section averaged over range from $q_{\min}$ to $q_{\max}$
$d_s$	3.5 (0.1)	cm	Sample thickness
$R_{\text{sn}}$	10.8 (8.1)		Calculated signal-to-noise ratio
$Ex_{\text{sn}}$	(9.6)		Measured signal-to-noise ratio

in Table 1. We calculate  $R_{\text{sn}}$  in the limit of low count rates using (Verwohlt *et al.*, 2018)

$$R_{\text{sn}} = \beta I_0 t_{\text{exp}} \exp(-1) \Lambda \left( \frac{1}{V} \frac{d\sigma}{d\Omega} \right) d\Omega_{\text{pix}} \left[ \frac{N_{\text{pix}} N_{\text{exp}}}{2(\beta + 1)} \right]^{1/2}. \quad (10)$$

Here  $\beta$  is the speckle contrast,  $I_0$  the incident X-ray flux,  $t_{\text{exp}}$  the exposure time,  $\Lambda$  the sample thickness,  $[(1/V)(d\sigma/d\Omega)]$  the scattering cross section per unit volume,  $d\Omega_{\text{pix}}$  the solid angle subtended by a detector pixel,  $N_{\text{pix}}$  the number of illuminated pixels and  $N_{\text{exp}}$  the number of camera exposures. The factor of  $\exp(-1)$  originates from absorption under the assumption the sample thickness is matched to the X-ray attenuation length.

We assume that the beam is focused to a 8 μm full width at half-maximum spot on the sample, so that the speckle size matches the detector pixel size of 76 μm at  $r_{\text{det}} = 12$  m. We take the sample thickness to be 3.5 cm so as to match the attenuation length of the X-ray beam at the incident energy of 23.7 keV. The fully coherent flux from a Si(311) monochromator is expected to be  $I_0 = 2.6 \times 10^{11}$  photons s<sup>-1</sup>, and we consider the average over all scattering within the  $q$ -range illuminated by the central ring of scattering (between  $q_{\min} = 0.35$  nm<sup>-1</sup> and  $q_{\max} = 0.50$  nm<sup>-1</sup>). In this region, the average intensity scattered into each detector pixel per 0.8 μs exposure comes out to be  $1.6 \times 10^{-5}$  photons. Finally, we assume the XSPA-500k camera is operated in burst mode with a duty cycle of 0.85%. Using equation (10) this configuration yields  $R_{\text{sn}} = 11$ . While the flux per pixel per exposure time is a very small number, we note that within a two hour measurement there are  $6.4 \times 10^{12}$  independent measurements within the specified  $q$ -range, so that the probability of counting coincidences is still appreciable. While burst mode can only record short data bursts, measurements in burst mode can be alternated by normal mode measurements which allows collection of a continuous data series out to the longest time set by the sample translation (Zhang *et al.*, 2018). In order to keep the beam damage below the threshold of 1.8 kGy

we need to translate the sample at a minimum velocity of 4.5 mm s<sup>-1</sup>, which sets a longest measurable delay time in the vicinity of 2 ms. Thus this configuration is expected to provide usable signal-to-noise ratios over three decades of time delays. Slower dynamics, if of interest, can be accessed by attenuating the beam.

## 5. Conclusions

In conclusion we have demonstrated that XPCS measurements of protein diffusion are compatible with continuous sample translation. The effects of motion on the correlation function can be corrected in a straightforward manner. Measurement of  $g_2$  over a

variety of sample translation speeds establishes a threshold dose for X-ray effects on diffusive dynamics of this highly concentrated protein solution, and this threshold is within a tolerable range.

The results of the present study should be applied to other systems with caution. The damage threshold could depend on many factors such as flux density, antioxidant concentration, antioxidant type, protein concentration and protein type. Damage could also depend on the time delay since irradiation, if the aggregation process of proteins is slow, or on the relative time scales of the intrinsic dynamics of the system to the slowing down due to damage. Further studies are needed to provide a fuller picture of these dependencies. However, the present study does provide confidence that XPCS measurements will be feasible at the higher fluxes available with diffraction-limited storage rings.

Scaling of the estimated  $R_{\text{sn}}$  to parameters appropriate to the upgraded APS-U indicates that sub-microsecond dynamics can be accessed using the current XSPA-500k detector even accounting for the greatly reduced duty cycle associated with burst mode. Thus studies of a wide range of biomaterials in the sub-microsecond to microsecond regime should become available with the opening of the APS-U.

## Acknowledgements

This research was performed on beamline 8-ID-I of the APS, a US Department of Energy (DOE) Office of Science User Facility operated for the DOE Office of Science by Argonne National Laboratory. We acknowledge the expert technical assistance of R. Ziegler and D. Jensen (APS) and O. Fraser (RIT).

## Funding information

Funding for this research was provided by: Department of Energy (contract No. DE-AC02-06CH11357). Laurence Lurio acknowledges the financial support from the X-ray Science Division, APS, for a visiting scientist position.

## References

- Allan, E. G., Kander, M. C., Carmichael, I. & Garman, E. F. (2013). *J. Synchrotron Rad.* **20**, 23–36.
- Blakeley, M. P., Hasnain, S. S. & Antonyuk, S. V. (2015). *IUCrJ*, **2**, 464–474.
- Brooks-Bartlett, J. C., Batters, R. A., Bury, C. S., Lowe, E. D., Ginn, H. M., Round, A. & Garman, E. F. (2017). *J. Synchrotron Rad.* **24**, 63–72.
- Busch, S., Jensen, T. H. Y. C., Chushkin, Y. & Fluerasu, A. (2008). *Eur. Phys. J. E*, **26**, 55.
- Chowdhury, D. P., Sorensen, C. M., Taylor, T. W., Merklin, J. F. & Lester, T. W. (1984). *Appl. Opt.* **23**, 4149–4154.
- Costa, L., Andriatis, A., Brennich, M., Teulon, J., Chen, S. W., Pellequer, J. & Round, A. (2016). *BMC Struct. Biol.* **16**, 18.
- Dix, J. A. & Verkman, A. S. (2008). *Annu. Rev. Biophys.* **37**, 247–263.
- Egerton, R. R. (2019). *Micron*, **119**, 72–87.
- Eriksson, M., van der Veen, J. F. & Quitmann, C. (2014). *J. Synchrotron Rad.* **21**, 837–842.
- Ferrell, R. T. & Himmelblau, D. M. (1967). *AIChE J.* **13**, 702–708.
- Fluerasu, A., Moussaïd, A., Falus, P., Gleyzolle, H. & Madsen, A. (2008). *J. Synchrotron Rad.* **15**, 378–384.
- Gabriel, J., Blochowicz, T. & Stühn, B. (2015). *J. Chem. Phys.* **142**, 104902.
- Garman, E. F. & Weik, M. (2015). *J. Synchrotron Rad.* **22**, 195–200.
- Garman, E. F. & Weik, M. (2017). *J. Synchrotron Rad.* **24**, 1–6.
- Garrison, W. M. (1987). *Chem. Rev.* **87**, 381–398.
- Griffith, W. L., Triolo, R. & Compere, A. L. (1987). *Phys. Rev. A*, **35**, 2200–2206.
- Grübel, G., Madsen, A. & Robert, A. (2008). In *Soft-Matter Characterization*, edited by R. Pecora. Heidelberg: Springer.
- Hopkins, J. B. & Thorne, R. E. (2016). *J. Appl. Cryst.* **49**, 880–890.
- Hunter, G. L. & Weeks, E. R. (2012). *Rep. Prog. Phys.* **75**, 066501.
- Jeffries, C. M., Graewert, M. A., Svergun, D. I. & Blanchet, C. E. (2015). *J. Synchrotron Rad.* **22**, 273–279.
- Kirby, N., Cowieson, N., Hawley, A. M., Mudie, S. T., McGillivray, D. J., Kusel, M., Samardzic-Boban, V. & Ryan, T. M. (2016). *Acta Cryst. D* **72**, 1254–1266.
- Kleczek, R., Kmon, P., Maj, P., Szczygiel, R., Grybos, P., Nakaye, Y., Sakumura, T. & Takeyoshi, T. (2019). *Proceedings of the IEEE 45th European Solid State Circuits Conference (ESSCIRC 2019)*, 23–26 September 2019, Krakow, Poland, pp. 85–88.
- Kuwamoto, S., Akiyama, S. & Fujisawa, T. (2004). *J. Synchrotron Rad.* **11**, 462–468.
- Lehny, R. L. (2012). *Curr. Opin. Colloid Interface Sci.* **17**, 3–12.
- Lhermitte, J. R. M., Rogers, M. C., Manet, S. & Sutton, M. (2017). *Rev. Sci. Instrum.* **88**, 015112.
- Massover, W. H. (2007). *J. Synchrotron Rad.* **14**, 116–127.
- Meisburger, S. P., Warkentin, M., Chen, H., Hopkins, J. B., Gillilan, R. E., Pollack, L. & Thorne, R. E. (2013). *Biophys. J.* **104**, 227–236.
- Möller, J., Sprung, M., Madsen, A. & Gutt, C. (2019). *IUCrJ*, **6**, 794–803.
- Polsinelli, I., Savko, M., Rouanet-Mehouas, C., Ciccone, L., Nencetti, S., Orlandini, E., Stura, E. A. & Shepard, W. (2017). *J. Synchrotron Rad.* **24**, 42–52.
- Ryan, T. M., Trehwella, J., Murphy, J. M., Keown, J. R., Casey, L., Pearce, F. G., Goldstone, D. C., Chen, K., Luo, Z., Kobe, B., McDevitt, C. A., Watkin, S. A., Hawley, A. M., Mudie, S. T., Samardzic Boban, V. & Kirby, N. (2018). *J. Appl. Cryst.* **51**, 97–111.
- Ryazantsev, S. N., Poliansky, N. B., Chebotareva, N. A. & Muranov, K. O. (2018). *Int. J. Biol. Macromol.* **117**, 1289–1298.
- Sandy, A. R., Zhang, Q. & Lurio, L. B. (2018). *Annu. Rev. Mater. Res.* **48**, 167–190.
- Shotton, M. W., Pope, L. H., Forsyth, V. T., Denny, R. C., Archer, J., Langan, P., Ye, H. & Boote, C. (1998). *J. Appl. Cryst.* **31**, 758–766.
- Singer, A. & Vartanyants, I. A. (2014). *J. Synchrotron Rad.* **21**, 5–15.
- Sinha, S., Jiang, Z. & Lurio, L. (2014). *Adv. Mater.* **26**, 7764–7785.
- Srinivas, P., Reddy, P. Y. & Reddy, G. B. (2008). *Biochem. J.* **414**, 453–460.
- Sutton, M. (2008). *C. R. Phys.* **9**, 657–667.
- Taylor, T. W. & Sorensen, C. M. (1986). *Appl. Opt.* **25**, 2421–2426.
- Thurston, G. M. (2006). *J. Chem. Phys.* **124**, 134909.
- Ueno, G., Shimada, A., Yamashita, E., Hasegawa, K., Kumasaka, T., Shinzawa-Itoh, K., Yoshikawa, S., Tsukihara, T. & Yamamoto, M. (2019). *J. Synchrotron Rad.* **26**, 912–921.
- UniProt (2019). *Nucleic Acids Res.* **47**, D506–D515.
- Van Holde, K. E., Johnson, W. C., Ho, P. S., *et al.* (2006). *Principles of Physical Biochemistry*. Upper Saddle River: Pearson/Prentice Hall.
- Verwohlt, J., Reiser, M., Randolph, L., Matic, A., Medina, L. A., Madsen, A., Sprung, M., Zozulya, A. & Gutt, C. (2018). *Phys. Rev. Lett.* **120**, 168001.
- Vodnala, P., Karunaratne, N., Lurio, L., Thurston, G. M., Vega, M., Gaillard, E., Narayanan, S., Sandy, A., Zhang, Q., Dufresne, E. M., Foffi, G., Grybos, P., Kmon, P., Maj, P. & Szczygiel, R. (2018). *Phys. Rev. E*, **97**, 020601.
- Vrij, A. (1979). *J. Chem. Phys.* **71**, 3267–3270.
- Wang, C., Lin, Y., Bougie, D. & Gillilan, R. E. (2018). *Acta Cryst. D* **74**, 727–738.
- Zhang, Q., Dufresne, E. M., Nakaye, Y., Jemian, P. R., Sakumura, T., Sakuma, Y., Ferrara, J. D., Maj, P., Hassan, A., Bahadur, D., Ramakrishnan, S., Khan, F., Veseli, S., Sandy, A. R., Schwarz, N. & Narayanan, S. (2021). *J. Synchrotron Rad.* **28**, 259–265.
- Zhang, Q., Dufresne, E. M., Narayanan, S., Maj, P., Koziol, A., Szczygiel, R., Grybos, P., Sutton, M. & Sandy, A. R. (2018). *J. Synchrotron Rad.* **25**, 1408–1416.